

Foucault pendulum on a chip: Rate integrating silicon MEMS gyroscope

Igor P. Prikhodko*, Sergei A. Zotov, Alexander A. Trusov, Andrei M. Shkel

MicroSystems Laboratory, Department of Mechanical and Aerospace Engineering, University of California, Irvine, CA, USA

ARTICLE INFO

Article history:

Received 8 May 2011

Received in revised form 6 October 2011

Accepted 16 January 2012

Available online 3 February 2012

Keywords:

MEMS gyroscope

Angle measuring

Whole angle

Rate integrating

Quality factor

Bandwidth

ABSTRACT

We report detailed characterization of a vacuum sealed rate integrating silicon MEMS gyroscope. The new gyroscope utilizes geometrically symmetric, dynamically balanced quadruple mass architecture, which provides a combination of maximized quality (Q) factors and isotropy of both the resonant frequency and damping. The vacuum sealed SOI prototype with a 2 kHz operational frequency demonstrated virtually identical X - and Y -mode Q -factors of 1.2 million. Due to the stiffness and damping symmetry, and low energy dissipation, the gyroscope can be instrumented for direct angle measurements with fundamentally unlimited rotation range and bandwidth. Experimental characterization of the mode-matched gyroscope operated in whole-angle mode confirmed linear response in a $\pm 450^\circ/\text{s}$ range and 100 Hz bandwidth (limited by the experimental setup), eliminating both bandwidth and range constraints of conventional open-loop Coriolis vibratory rate gyroscopes.

© 2012 Elsevier B.V. All rights reserved.

1. Introduction

In the past decade micromachined vibratory gyroscopes have received increased attention from automotive and consumer electronics industries. All commercial MEMS gyroscopes are angular rate measuring sensors employing energy transfer from the closed-loop drive to the secondary sense-mode [1]. The resolution and sensitivity of MEMS gyroscopes are often improved by maximizing Q -factors and reducing frequency mismatch between the two modes of vibration [2]. Mode-matched silicon gyroscopes with Q above 100,000 have been demonstrated to provide sub-degree-per-hour bias stability in a limited measurement bandwidth [3–5]. Improvement of rate bandwidth is typically addressed by operating the sense-mode in a closed loop, or force-rebalance mode [6]. The trade-off however is the noise increased by a closed loop gain, as well as the limited range of an input rate defined by the feedback voltage required to rebalance the proof-mass.

An alternative to the force-rebalance electronic architecture is the whole-angle mode of operation, which provides fundamentally unlimited input range and measurement bandwidth [6]. The whole-angle, or rate integrating mode allows to measure the angular position or orientation of an object directly from the proof-mass motion, without numerical integration of an angular rate signal. The angle output is useful for inertial navigation, azimuth (North direction) tracking [5], and orientation setting in dead-reckoning and targeting systems, especially in GPS-denied environments [7]. In

addition, the whole-angle mode has an extremely accurate angular gain factor, which to the first order is independent of material properties or electronics, and defined purely by the geometry of a proof-mass [8].

To enable whole-angle measurements, sensor requirements for structural symmetry and Q -factors are more stringent than for rate measurements, and call for new design architectures. For instance, the macro-scale hemispherical resonator gyroscope (HRG) with sub-arc-second angle resolution requires isotropic Q -factors as high as 26 million [8]. Achieving this level of damping and stiffness symmetry (e.g. 10^{-4} Hz) across process variations of conventional silicon MEMS technologies is very challenging. To implement a rate integrating gyroscope in silicon MEMS, a lumped mass design was first introduced in [9], and later feasibility of the approach was demonstrated in [10]. Recently, we also proposed the interchangeable rate and whole-angle operation [11], making one mechanical structure suitable for high precision and wide range measurements.

The latest advances in design [12] and packaging of silicon MEMS devices [13,11] enabled vibratory gyroscopes with Q -factors above 0.5 million and energy decay time constants of at least 1 min. High Q -factors and long dissipation times inspired the development of angle measuring MEMS gyroscopes based on free vibrations [14]. While final realization of an angle measuring concept may require closed loop to sustain energy [10,15–21] for operating times exceeding several minutes, in this paper we present the first experimental demonstration of the direct angle measurements in free vibrations. Fig. 1 shows the vacuum sealed quadruple mass gyroscope (QMG) with isotropic dissipation constant of 3 min used for the experimental demonstration.

* Corresponding author.

E-mail address: igor.prikhodko@gmail.com (I.P. Prikhodko).

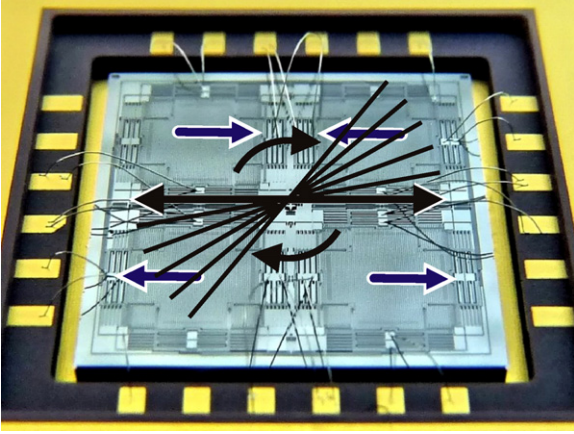


Fig. 1. Photograph of a fabricated 100 μm thick SOI quadruple mass gyro (QMG) with the illustration of the whole-angle operation.

Section 2 introduces the whole-angle operating principles and the error model of an angle measuring gyroscope. In Section 3 we discuss the QMG design, structural parameters, fabrication and vacuum packaging. Section 4 describes detection algorithms and electronics for real-time angle measurements. Structural, thermal, and angle measurement characterization of the sensor are introduced in Section 5, followed by a bandwidth comparison for whole angle and rate measuring modes. Section 6 concludes the paper with a summary of results. Appendix A reviews the dynamics of the rate integrating gyroscope (Foucault pendulum) for both ideal and non-ideal cases.

2. Whole-angle mode of operation

In this section we describe the operating principle and the fundamental error model for an angle measuring gyroscope.

2.1. Operating principle

An ideal angle measuring vibratory gyroscope is a 2-D isotropic mass-spring system vibrating with the natural frequency ω . In presence of the inertial rotation with the rate Ω , the equations of motion in terms of x , y displacements are (relative to a gyroscope non-inertial frame) [6]:

$$\begin{aligned} \ddot{x} + (\omega^2 - k^2\Omega^2)x - k(2\Omega\dot{y} + \dot{\Omega}y) &= 0, \\ \ddot{y} + (\omega^2 - k^2\Omega^2)y + k(2\Omega\dot{x} + \dot{\Omega}x) &= 0, \end{aligned} \quad (1)$$

where k is the angular gain factor defined by the geometric structure of the gyroscope. Theoretical maximum for the geometric constant is $k=1$. The centrifugal Ω^2 and angular acceleration $\dot{\Omega}$ terms are included to account for the bandwidth and wide range of input rotations. The dynamics of Eq. (1) also assumes negligible damping and free vibrations, which can be achieved for gyroscopes with high Q -factors and long energy dissipation time constants. The dynamics of a non-ideal gyroscope is summarized in Section 2.2 and Appendix A.

As shown in Appendix A, the general solution of Eq. (1) is either a straight line or an orbital (elliptical) trajectory motion in x - y plane with parameters a , q , θ_0 , ϕ , describing semi-major, semi-minor axes, the initial inclination angle, and the orbital phase, respectively, Fig. 2. The parameters a and q can be thought of as the amplitude and the quadrature of the proof-mass motion in x - y

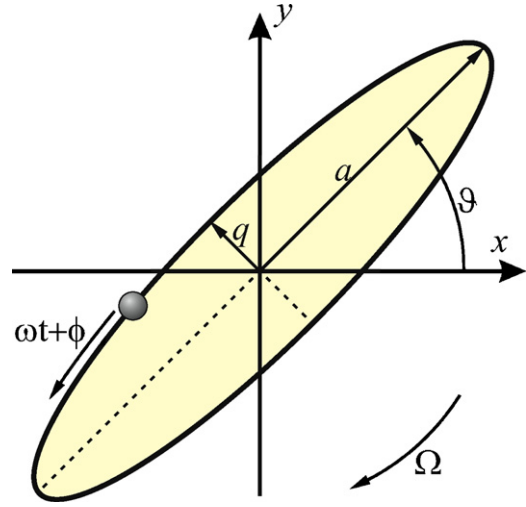


Fig. 2. Orbital trajectory of a proof-mass motion in response to the inertial rate Ω , showing the amplitude and quadrature a , q , the inclination angle θ , the vibration frequency and phase ω , ϕ in x - y plane.

plane. For a straight line oscillation (zero quadrature $q=0$) the solution simplifies to:

$$\begin{aligned} x &= a \cos \left(\theta_0 - k \int_{t_0}^t \Omega(\tau) d\tau \right) \cos(\omega t + \phi), \\ y &= a \sin \left(\theta_0 - k \int_{t_0}^t \Omega(\tau) d\tau \right) \cos(\omega t + \phi), \end{aligned} \quad (2)$$

which shows that in presence of inertial rotation, the vibration pattern precesses with the angular rate $-k\Omega$ relative to the gyroscope's reference frame. In other words, the variable inclination (precession) angle θ of the orbital trajectory is proportional to the orientation angle of a gyroscope:

$$\theta = \theta_0 - k \int_0^t \Omega(\tau) d\tau, \quad (3)$$

which holds for arbitrary initial conditions, see Appendix A. As follows from Eq. (2), the instantaneous changes in the precession angle θ can be detected by monitoring x , y read-out signals according to:

$$\theta = \arctan \left(\frac{y}{x} \right). \quad (4)$$

Angle detection algorithms for the general case are presented in Section 4.

Eq. (3) describes the governing principle for the whole-angle operation (rate integrating). The whole-angle mode is based upon the classical Foucault pendulum operation, where the axis of vibration is allowed to precess freely in response to the inertial rotation, Fig. 3. For the ideal case with $q=0$, $k=1$, Fig. 3(a), an orientation of the free vibrating axis remains fixed in the inertial space, thereby providing an instantaneous orientation reference. The gyroscope's precession angle in this case is equal to the angle of input rotation. This principle was first discovered by Bryan in 1890 [22] for wine glass structures ($k=0.3$) that are used now for inertial grade gyroscopes, such as HRG. Unlike the conventional rate measuring mode, where the axis of vibration is effectively locked to the intended drive direction, Fig. 3(b), the whole-angle mode poses no fundamental limitation to the input range or bandwidth [6]. This can be explained by the free, unconstrained motion of the proof-mass. The ultimate maximum of the rotation rate and measurement bandwidth is defined by the resonant frequency of the device, which is typically on the order of 1–10 kHz (hundreds

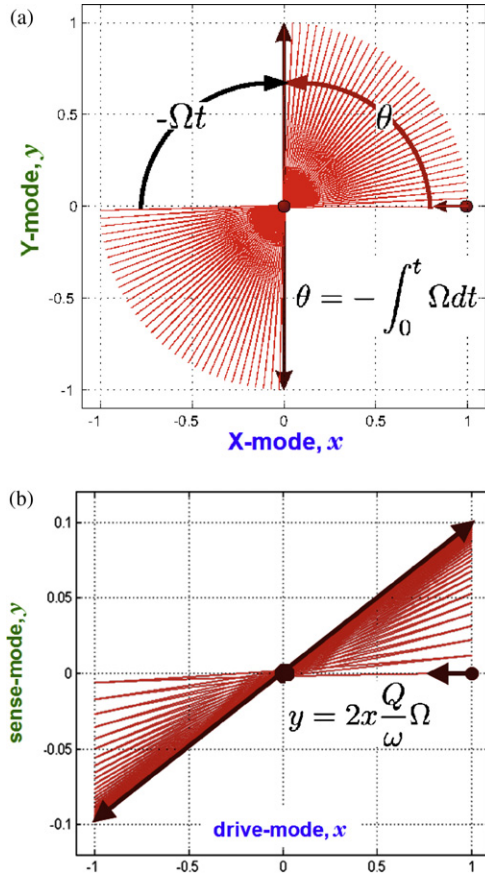


Fig. 3. Conceptual demonstration of the conventional rate and angle measuring modes in x - y plane, simulations. While the proof-mass oscillations are free and unconstrained in the whole-angle operation, the motion is effectively locked to the intended drive direction (x -axis) in the rate mode. (a) Whole-angle (rate integrating) mode: precession of the vibration axis in response to an inertial rotation, with the precession angle equal to the rotation angle. (b) Conventional rate mode: sense-mode oscillations induced by an inertial rotation, with the amplitude proportional to the angular rate. The y -axis scale differs.

of thousands degrees per second) for silicon MEMS vibratory gyroscopes.

2.2. Whole-angle gyroscope error model

The above conceptual analysis of the whole-angle operating mode assumes isotropic stiffness and negligible damping. The angle drift in presence of imperfections was derived in [6,23] by the method of averaging, and summarized in Appendix A. For mismatches $\Delta\omega = (\omega_1^2 - \omega_2^2)/(2\omega)$ in frequencies $\Omega_{1,2}$, and $\Delta(1/\tau) = 1/\tau_1 - 1/\tau_2$ in energy dissipation time constants $\tau_{1,2}$, the angle drift for non-ideal gyroscope is:

$$\dot{\theta} = -k\Omega + \frac{1}{2} \Delta \left(\frac{1}{\tau} \right) \sin 2(\theta - \theta_\tau) + \Delta\omega \cos 2(\theta - \theta_\omega) \frac{aq}{a^2 - q^2}, \quad (5)$$

where $\theta_\tau, \theta_\omega$ are the angle differences between the x and y pick-off axes and principal axes of τ_1 damping and Ω_2 elasticity, respectively. This equation reveals the periodic nature of the angle drift; errors are averaged out for fast spinning objects. The minimum detectable angle derived from Eq. (5) is limited by the mismatches in device damping and frequency:

$$|\dot{\theta}_{\text{drift}}| \leq \frac{1}{2} \left| \Delta \left(\frac{1}{\tau} \right) \right| + \frac{q}{a} |\Delta\omega|. \quad (6)$$

In practice, the term $(q/a)|\Delta\omega|$ is compensated either by electrostatic or mechanical trimming of stiffness asymmetry [24] to null $\Delta\omega$ or by quadrature control to null q [17,19].

In contrast, the damping asymmetry is the major drift source in angle measuring MEMS, and requires highly isotropic Q -factors to overcome this limitation. According to Eq. (5) with $\Delta\omega = 0$, presence of the term $\Delta(1/\tau)$ results in a false precession of the gyroscope $\dot{\theta} \neq 0$ for zero input $\Omega = 0$. Different decay time constants for each x and y direction, e.g. $\tau_1 > \tau_2$, cause the vibrating axis to swing toward the axis of least damping, τ_2 . The rate of this drift is defined by the damping mismatch $\Delta(1/\tau)$, which determines the ultimate performance of the sensor.

The damping mismatch $\Delta(1/\tau)$ can be also presented in terms of the Q -factor mismatch $\Delta Q/Q$ and the average time constant τ :

$$\Delta \left(\frac{1}{\tau} \right) = \frac{1}{\tau_1} - \frac{1}{\tau_2} = \frac{\Delta Q}{Q} \frac{1}{\tau}, \quad (7)$$

showing that the damping mismatch-induced error can be further reduced by maximizing Q or τ . The error analysis suggests that mismatches in frequency (aniso-elasticity) and energy decay time constants (aniso-damping) often arising from fabrication imperfections and packaging are the main factors limiting realization of angle measuring gyroscopes. These considerations motivate the development of a fully symmetric gyroscope with ultra-high Q -factors for low angle drift operation.

2.3. Comparison with conventional rate measuring mode

Foucault pendulum-type devices can be also operated in the conventional rate mode. For rate measurements, the proof-mass is continuously driven by a periodic force into a steady-state resonant motion along the drive x -axis. As opposed to the free vibrations in whole-angle mode, forced vibrations in rate mode effectively lock the motion to the intended drive-mode direction. While the drive-mode motion is controlled by a closed loop, the sense-mode motion is induced by the inertial rotation only, Fig. 3(b). At relatively slow input rotation, the ratio of sense- to drive-mode amplitudes is a measure of the inertial rate [23]:

$$\frac{|y|}{|x|} = 2k \frac{Q}{\omega} \frac{1}{\sqrt{1 + 4Q^2(\Delta\omega/\omega)^2}} \Omega. \quad (8)$$

Although dynamics and instrumentation are different for rate and whole-angle modes, the required structural parameters for low noise operation are similar. As follows from Eq. (8) rate sensitivity also benefits from Q -factor maximization, high angular gain k , and zero frequency mismatch $\Delta\omega = 0$, which are easier achieved for symmetric structures (e.g. HRG and QMG).

While rate noise performance improves in rate mode with higher Q , the trade-off is a limited open-loop input range and measurement bandwidth. The potential solution is an interchangeable operation between the forced vibrations (rate mode) and free precession (angle measuring mode), which was recently demonstrated for QMG [11,37]. The detailed noise characterization of the QMG in rate measuring mode revealed a sub-degree per hour bias instability [4,5], which combined with the measured $\pm 18,000^\circ/\text{s}$ input range in free vibrations provides the dynamic range of at least 157 dB [25].

3. Transducer design and instrumentation

In this section we report the QMG transducer design, structural parameters, fabrication and vacuum packaging.

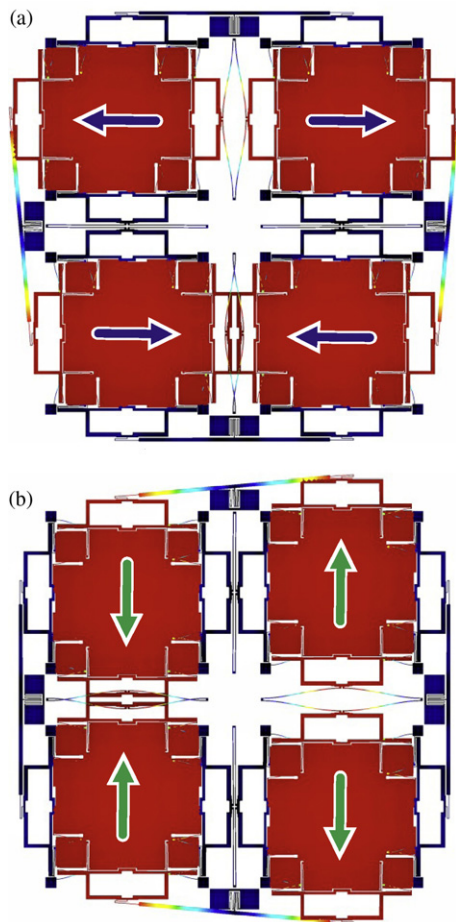


Fig. 4. Degenerate, anti-phase X- and Y-vibratory modes of dynamically balanced QMG, finite element modeling. Anti-phase motion of each pair of tines is synchronized by the integrated mechanical lever mechanisms. (a) X-mode of vibration. (b) Y-mode of vibration.

3.1. Transducer design concept

The novel z-axis MEMS angle measuring sensor utilizes a symmetric quadruple mass architecture recently introduced in [11]. The QMG sensor structure is comprised of four symmetrically decoupled tines that are synchronized by anti-phase lever mechanisms, Fig. 4. The sensor can be thought of as two levered tuning fork gyroscopes, whose anti-phase motion reduces the substrate energy dissipation (anchor loss) and maximizes Q-factors. In addition to improved energy dissipation and isotropy, lever mechanisms provide vibration isolation and suppress temperature drifts. Each of the four tines is an isotropic resonator consisting of a square proof mass suspended by two X-mode and two Y-mode decoupling shuttles, which are restricted to move in either X or Y direction [26]. This design enables whole-angle mode based on free vibrations of the proof-mass, with the precession angle proportional to the rotation angle.

The vibration pattern of the QMG is a superposition of the two geometrically identical modes of vibration. In contrast to the conventional tuning fork design [27–29] with in-plane drive-mode and out-of-plane sense-mode, both X- and Y-modes of QMG are in-plane of the substrate, making the gyroscope input sensitive to out-of-plane rotations. Due to symmetry, X- and Y-modes are degenerate and spatially oriented at a 90° angle. Precession of the vibration pattern results from the inertial rotation, which causes energy transfer between the X- and Y-modes. The precession angle is measured from the projection of the vibration pattern on each

axis. This is accomplished by the capacitive electrodes located on each side of the decoupling shuttles. Even though electrodes may potentially actuate and detect motion in both direction due to fabrication imperfections, the decoupling shuttles/frames proposed in [26] ensure motion strictly in one direction. The angular gain factor, defined as the ratio of the precession angle to the rotation angle, is thus less than its theoretical maximum of 1 because the motion of the shuttles are not affected by the Coriolis acceleration. The expression for the angular gain can be derived by subtracting the mass of each shuttle m_{sh} from the total mass M in the Coriolis term of the two-dimensional oscillator with stiffness K :

$$\begin{aligned} M\ddot{x} + Kx - 2(M - 2m_{sh})\Omega\dot{y} &= 0, \\ M\ddot{y} + Ky + 2(M - 2m_{sh})\Omega\dot{x} &= 0. \end{aligned} \quad (9)$$

Here, the centrifugal Ω^2 and angular acceleration $\dot{\Omega}$ terms are neglected for simplicity. After normalization of Eq. (9), we obtain the Coriolis term coefficient:

$$k = 1 - \frac{2m_{sh}}{M}, \quad (10)$$

which for the first generation QMG layout shown in Fig. 4 is approximately $k = 0.88$. The angular gain factor is defined by the geometry of the inertial mass, and to the first order independent of its material properties, thus providing an improved stability [8].

3.2. Sensor structural parameters

While design parameters of the QMG are discussed in details in [37], here we highlight the structural properties critical for the whole-angle mode realization. In comparison to the precision machined axisymmetric HRG, previously investigated silicon MEMS gyroscopes suffered from aniso-elasticity, aniso-damping, and short energy dissipation constant (less than 1 s). As follows from the error model in Section 2.2, maximization of Q-factor is critical for the whole-angle operation. The Q-factor in vibratory MEMS is governed by viscous (air) damping, thermoelastic dissipation (TED), anchor and surface losses [30,31]; these effects should be minimized on both design and packaging levels. The developed packaging technology [13] for robust vacuum sealing of high-Q gyroscope ensures less than 0.1 mTorr pressure environment inside the package cavity by using activated getters, eliminating viscous damping. The balanced tuning fork design of QMG with linear flexures and anti-phase lever mechanisms provides low anchor loss. The dominant energy loss mechanism in all vacuum sealed QMGs is the thermoelastic damping, which was experimentally confirmed in [4,11]. Based on FEM analysis, the fundamental TED limit of 1.35 million (energy time constant of 195 s) was estimated for a silicon QMG design with a 2.2 kHz typical resonant frequency, which provides at least 10 min of sensor's operating time until the amplitude decays to 5% of its initial value.

While whole-angle operation is theoretically possible for gyroscopes with different X- and Y-modes [23], the performance significantly improves for symmetrical structures with identical vibratory modes. Analysis of Eq. (6) suggests decreased angle drift for isotropic damping $\Delta(1/\tau) = 0$ and frequency $\Delta\omega = 0$. The design goal of matching frequencies of X- and Y-modes (over temperature) is already satisfied in QMG architecture due to the structural symmetry. Further post-fabrication frequency matching is possible by electrostatic tuning or mechanical trimming [24]. Most importantly, the geometrical symmetry enables closer match of Q-factor values along X- and Y-directions, which is generally more challenging task. The QMG design is expected to enable whole-angle mode of operation due to advantageous combination of low energy dissipation and isotropy of both the resonant frequency and the damping.

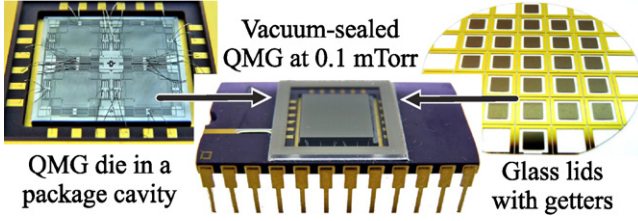


Fig. 5. Photograph of a stand-alone vacuum packaged QMG prototype lid sealed at 0.1 mTorr with getter material.

3.3. Prototype fabrication and vacuum packaging

The QMG prototypes, Fig. 5, used in the experimental study were fabricated using an in-house, wafer-level, single-mask process based on silicon-on-insulator (SOI) substrates with a conductive 100 μm thick device layer and a 5 μm buried oxide layer. Sensors were defined in a highly doped (boron concentrations of 10^{20} cm^{-3}) device layer by DRIE using a Unaxis Versaline VL-7339 tool. The minimum feature size of the overall process used to define the capacitive gaps was 5 μm . The singulated gyroscopes were then released using a timed 20% hydrofluoric (HF) acid bath. To obtain stand-alone high-Q transducers, the dies were attached to 24-pin DIP ceramic packages using Au–Sn eutectic solder preforms followed by wire bonding. Finally, the devices were sealed at 0.1 mTorr vacuum, preceded by the getter activations on custom-made glass lids.

4. Interface electronics and angle detection algorithms

In this subsection we describe read-out electronics and detection algorithms implemented for direct real-time angle measurements.

4.1. Front end electronics

All experiments were performed using a custom PCB connected to a FPGA-based HF2LI unit from Zurich Instruments. The vacuum packaged sensor was mounted on a PCB with front-end transimpedance amplifiers and installed on the 1291BR Ideal Aerosmith rate table, which was enclosed in a thermal chamber. Electrostatic actuation and capacitive detection were employed along with the electromechanical amplitude modulation (EAM) [32] for the parasitic feedthrough elimination, depicted as a carrier and sideband demodulation in block diagram Fig. 6. All control and signal processing were realized using a LabView programmable HF2LI unit.

4.2. Angle detection overview

A brief overview of the previously reported angle detection methods below provides a comparison with the algorithm implemented in Section 4.3. The methods proposed in [15,6,19] assume an external reference generator of the frequency ω close to the gyroscope's natural frequency. The classical method for the angle detection was proposed by Friedland and Hutton [15]. The precession angle is computed from real-time displacements $x(t)$, $y(t)$, and velocities $\dot{x}(t)$, $\dot{y}(t)$:

$$\theta(t) = \frac{1}{2} \arctan \frac{2(\omega^2 xy + \dot{x}\dot{y})}{\omega^2(x^2 - y^2) + (\dot{x}^2 - \dot{y}^2)}, \quad (11)$$

which holds true for ideal gyroscope dynamics. The potential challenge of this approach is the derivation of $\dot{x}(t)$, $\dot{y}(t)$ velocities from $x(t)$, $y(t)$ read-out (pick-off) signals, which adds noise and additional post-processing complexity.

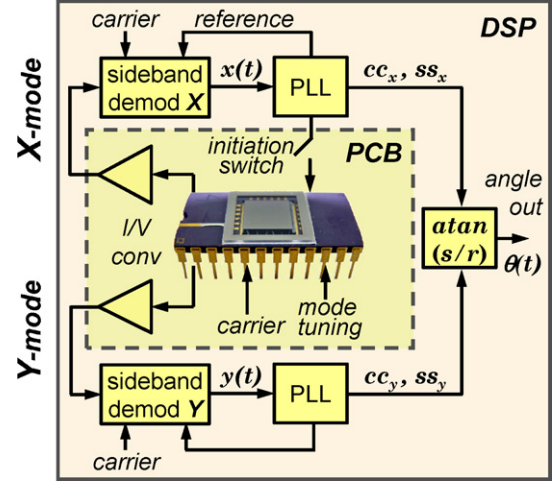


Fig. 6. Block diagram of QMG signal processing for real-time angle measurements.

For non-ideal dynamics in presence of quadrature ($q \neq 0$) the angle extraction is possible by amplitude demodulation of read-out signals at the reference frequency ω and phase ϕ [19]:

$$\theta(t) = \arctan \frac{\text{LPF}[y \cos(\omega t + \phi)]}{\text{LPF}[x \cos(\omega t + \phi)]}, \quad (12)$$

where $\text{LPF}(\cdot)$ denotes low pass filtering of the signal.

Both estimations Eqs. (11) and (12) require a control loop to lock an external reference frequency to the gyroscope natural frequency. An alternative approach proposed by Lynch in [6] is to use invariant quantities:

$$\begin{aligned} S &= 2(c_x c_y + s_x s_y) = ((a^2 - q^2)/4) \sin 2\theta, \\ R &= c_x^2 + s_x^2 - c_y^2 - s_y^2 = ((a^2 - q^2)/4) \cos 2\theta, \end{aligned} \quad (13)$$

computed from the demodulated pick-off signals:

$$\begin{aligned} c_x &= \text{LPF}[x \cos(\omega t + \phi)], & s_x &= \text{LPF}[x \sin(\omega t + \phi)], \\ c_y &= \text{LPF}[y \cos(\omega t + \phi)], & s_y &= \text{LPF}[y \sin(\omega t + \phi)], \end{aligned} \quad (14)$$

to extract the precession angle:

$$\theta(t) = \frac{1}{2} \arctan \frac{S}{R}. \quad (15)$$

Here we adopt this concept and utilize the quadratic combinations of demodulated components for the angle calculation. The method Eq. (15) is analogous to Eq. (11), but robust to slight variations between the gyroscope phase and an external reference. This is possible because the phase difference can be recovered from the demodulated components Eq. (14), see [6].

4.3. Back end electronics and algorithms

The angle detection method implemented in this work takes advantage of the QMG high Q-factors to maximize signal-to-noise ratio. Similar to the concept described in [6], the demodulated components of read-out signals are used for angle calculation. The method employs a phase-locked loop (PLL) to track natural frequency of a device and generate a reference signal for demodulation. The high-Q factor implicates a steep slope of the phase response curve, which makes frequency (phase) tracking and demodulation more accurate. Signal processing depicted in Fig. 6 assumes operation of a gyroscope in free vibrations, with decay time constants determined by the Q-factors. To initiate vibrations, the QMG is electrostatically driven into the X-mode anti-phase

resonant motion using a PLL. The initialization parameters are discussed in Section 5.2.1. The angle measurements are performed with an excitation force turned off to ensure free and unconstrained motion of the proof-mass. Maximization of the energy dissipation time constant in whole-angle mode, is therefore, extremely critical. For example, Q -factor of 1 million provides 6 min of operating time for a 2 kHz device, until the amplitude of vibrations decays to 10% of its initial value. As shown in A.2, free decay does not affect angle measurements as long as both frequency and damping are closely matched. For a continuous operation of a practical sensor system, the energy of the system can be sustained by the parametric excitation [20] or other controls [6,10,15–19,21] without affecting the orientation of the vibrating axis. Fig. 6 shows the detection scheme implemented for real-time angle measurements. Using trigonometric identities, the x, y pick-off signals Eq. (A.6) transforms to:

$$\begin{aligned} x &= \frac{a+q}{2} \cos \left(\omega t - k \int_0^t \Omega dt + \phi \right) \\ &\quad + \frac{a-q}{2} \cos \left(\omega t + k \int_0^t \Omega dt + \phi \right), \\ y &= \frac{a+q}{2} \sin \left(\omega t - k \int_0^t \Omega dt + \phi \right) \\ &\quad - \frac{a-q}{2} \sin \left(\omega t + k \int_0^t \Omega dt + \phi \right). \end{aligned} \quad (16)$$

Analysis of Eq. (16) shows that the spectrum of x, y signals contains two frequency components, $\Omega \pm k\Omega$, which can be employed for differential angular rate estimation in real-time [33]. The PLL employed in Fig. 6 locks the reference generator to the frequency $(\omega - k\Omega)$ and phase ϕ , as well as generates the 0° and 90° shifted references. The amplitude demodulation of x and y pick-off signals is performed:

$$\begin{aligned} cc_x &= \text{LPF} \left[x \cos \left(\omega t - k \int_0^t \Omega dt + \phi \right) \right], \\ cc_y &= \text{LPF} \left[y \cos \left(\omega t - k \int_0^t \Omega dt + \phi \right) \right], \\ ss_x &= \text{LPF} \left[x \sin \left(\omega t - k \int_0^t \Omega dt + \phi \right) \right], \\ ss_y &= \text{LPF} \left[y \sin \left(\omega t - k \int_0^t \Omega dt + \phi \right) \right], \end{aligned} \quad (17)$$

to compute the quadratic invariants

$$\begin{aligned} s &= 2(cc_x cc_y + ss_x ss_y) = \frac{a^2 - q^2}{4} \sin \left(-2k \int_0^t \Omega dt \right), \\ r &= cc_x^2 + ss_x^2 - cc_y^2 - ss_y^2 = \frac{a^2 - q^2}{4} \cos \left(-2k \int_0^t \Omega dt \right), \end{aligned} \quad (18)$$

and obtain instantaneous values of the precession angle:

$$\theta(t) = \frac{1}{2} \arctan \frac{s}{r} = -k \int_0^t \Omega dt. \quad (19)$$

Fig. 6 scheme was implemented in LabView for real-time angle measurements reported in Section 5.2. The proposed signal processing allows to track the gyroscope frequency (and phase) with a millihertz resolution as required for high- Q sensors, providing an accurate demodulation and angle calculation. Relative calibration of x and y read-out signals was performed to avoid different gains (scaling) caused by variations of electronic components.

As discussed in Section 2, the measurement bandwidth of an angle measuring gyroscope is fundamentally unlimited due to the unconstrained free vibrations (as long as the natural frequency is greater than the input rotation rate). In practice, however, most angle detection methods Eqs. (12), (15) and (19) reduce the bandwidth value to the cut-off frequency of the low-pass filter (on the order of 100–200 Hz to track rapid changes of input rotation Ω). Depending on the application, the filter is tuned to provide optimum noise performance without sacrificing the measurement bandwidth.

5. Experimental characterization

In this section we experimentally evaluate structural symmetry and whole-angle operation of the QMG prototype. For the fundamental concept study all experiments presented here were performed using a vacuum sealed QMG operated in free decay regime, Fig. 5.

5.1. Structural characterization

The dynamically balanced, geometrically symmetric design of the QMG is expected to provide identical and high Q -factors. The damping symmetry of a stand-alone QMG prototype was investigated using ring-down tests. The time-domain amplitude decays of X - and Y -modes were fitted with exponential decays to extract time constants τ of 172 s and 174 s, respectively, Fig. 7. The Q -factors were calculated according to $Q = \pi f_n \tau$, with natural frequencies f_n of 2.2 kHz, Fig. 6. Experimentally measured X -mode Q of 1.16 and Y -mode Q of 1.18 million approach the fundamental thermoelastic limit of 1.35 million computed using FEM analysis in COMSOL. Structural characterization revealed virtually identical X - and Y -mode time constants of $173 \text{ s} \pm 0.5\%$, providing at least 10 min operating time in the free vibrations regime. The temperature characterization also revealed isotropic Q -factors above 0.7 million up to $+100^\circ\text{C}$ for a packaged QMG, Fig. 7 inset. The data confirms the design hypothesis of the inherent Q -factor symmetry in QMG structures.

To confirm linear operation, the Q -factor values were measured for vibration amplitudes ranging from 15 nm up to $1 \mu\text{m}$ (relative to the capacitive gaps of $5 \mu\text{m}$). Ring-down experimental test performed for different initial amplitudes, Fig. 8 confirmed negligible dependence of Q -factor on the vibration amplitude, thereby mak-

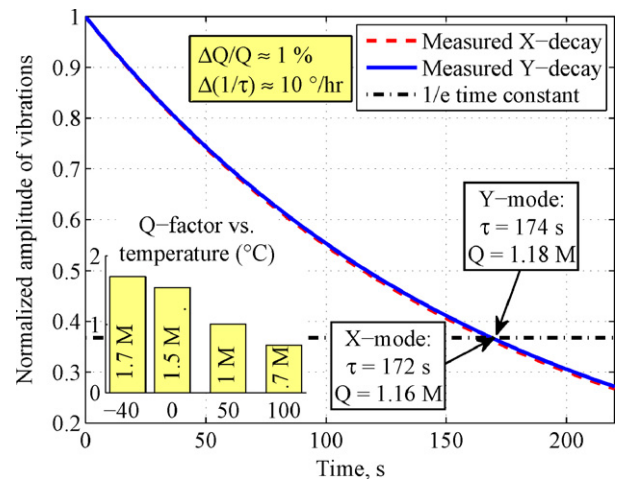


Fig. 7. Experimental characterization of the vacuum sealed QMG using ring-down tests. X -mode Q -factor of 1.16 and Y -mode Q of 1.18 million approach the fundamental thermoelastic limit of 1.35 million. Inset: measured Q -factor (million) vs. temperature in the range -40 to 100°C .

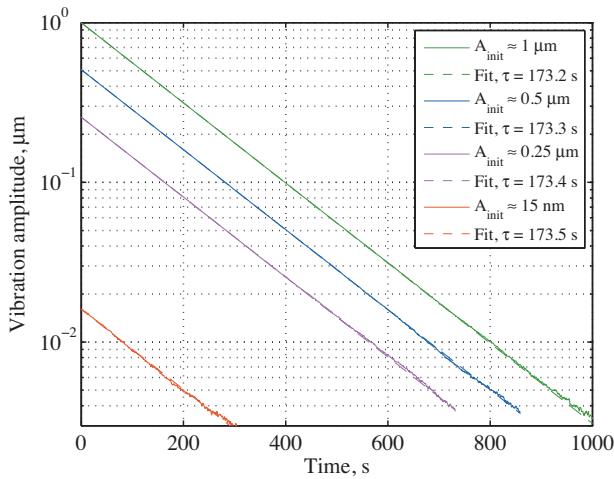


Fig. 8. Ring-down experimental measurements performed for different initial amplitudes (log scale), confirming negligible dependence of Q -factor on the vibration amplitude and at least 10 min of operation time in free decay.

ing possible operation in free decay without affecting the device linearity.

As discussed in Section 2.2, the damping asymmetry is a major error source for angle measuring gyroscopes. Fig. 10 shows drift rates for typical gyroscope structures (tuning fork, disk, and lumped quadruple design) based on the error model described by Eq. (5). For the QMG design, the measured mismatch $\Delta(1/\tau)$ of $10^\circ/\text{h}$ with the average τ of 173 s (equivalently, $\Delta Q/Q$ of 1% with Q of 1.17 million) leads to the drift of $1^\circ/\text{h}$ when operated in the whole-angle mode. Further improvements are possible by optimizing fabrication and packaging to reduce damping asymmetry. In comparison to other silicon structures, QMG architecture demonstrates the potential for whole-angle instrumentation with fundamentally unlimited input range and bandwidth.

5.2. Whole-angle mode characterization

Both the damping symmetry and the high Q -factors are expected to allow whole-angle measurements. We performed series of experiments to evaluate the QMG response to (i) rotation with a constant angular rate, (ii) accelerated rotation, and (iii) sinusoidal rotations to determine bandwidth.

5.2.1. Initialization

The angle measuring sensor can be implemented either in free vibrations or in closed loop to sustain vibrations, depending on the required operating time. For the experimental demonstration of the fundamental principle of operation, the angle measurements were performed using the stand-alone QMG operated in free vibrations. To initiate vibrations, the sensor with a 2.2 kHz operational frequency was electrostatically driven into the X-mode anti-phase resonant motion using the PLL until the amplitude reached $0.25 \mu\text{m}$ (or 5% of the nominal gap), and then abruptly turned off. For initial characterization, the frequency match of below 20 mHz between the X- and Y-modes ($\Delta f/f$ of 10 ppm) was then achieved by the electrostatic tuning, Fig. 9. While the initial mismatch was 3.6 Hz ($\Delta f/f$ of 1.5%), the tuning voltage was applied to the set of central parallel plates in x direction until the negative spring effect reduced X-mode resonant frequency to the value comparable with the Y-mode frequency at 17.15 Vdc. The active frequency tuning controls [19,10,34,38] are preferred for the final realization of the control electronics. As pointed out in Section 4.3, the gyroscope response to inertial stimulus is unaffected by the free decay as long as damping asymmetry and frequency mismatch are minimized.

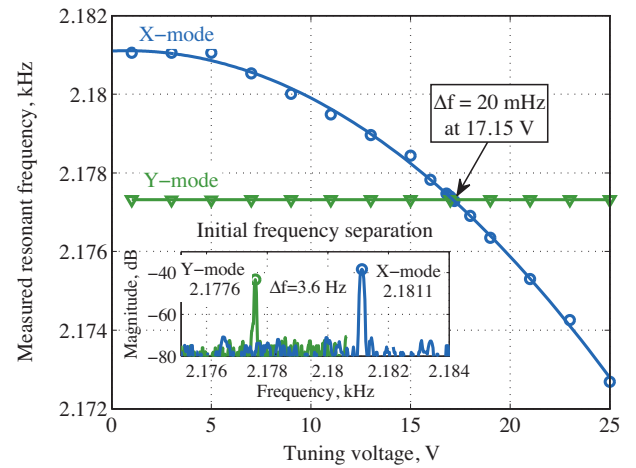


Fig. 9. Measured electrostatic frequency tuning of X-mode to the Y-mode frequency. A 20 mHz matching ($\Delta f/f$ of 10 ppm) is achieved by applying 17.15 Vdc. Inset: power spectrum density of X- and Y-modes before tuning, revealing an initial frequency separation $\Delta f/f$ of 0.15%.

Considering relatively low damping asymmetry ($\Delta Q/Q$ of 1%) and frequency mismatch ($\Delta f/f$ of 10 ppm), the gyroscope dynamics can be assumed ideal on the time scale of several minutes. The angle drift Eq. (5) due to the quadrature is reduced by the electrostatic tuning (depicted as tuning in Fig. 6), which is also implemented in the current setup, Fig. 9.

5.2.2. Response to constant rotation

To obtain an accurate estimate of the input inertial rate, we determined the actual angular gain factor from the input-output characteristics of the QMG sensor. The device was rotated with a constant angular rate of $100^\circ/\text{s}$. The instantaneous position of the axis of vibration was detected capacitively by monitoring the displacement of X- and Y-modes. The angle response in Fig. 11 was obtained in this experiment using the real-time detection scheme depicted in Fig. 6.

Fig. 11(a) shows two demodulated components s and r during a $100^\circ/\text{s}$ rotation, which were used for the angle computation. The recorded signals satisfy $\cos(2k\Omega t)$ and $\sin(2k\Omega t)$ relation between X- and Y-modes, as derived in Eq. (18). Fig. 11(b) shows the gyroscope output angle $\theta = \arctan(s/r)/2$ compared to the rate table reference. The linear fit to the measured data revealed $87^\circ/\text{s}$

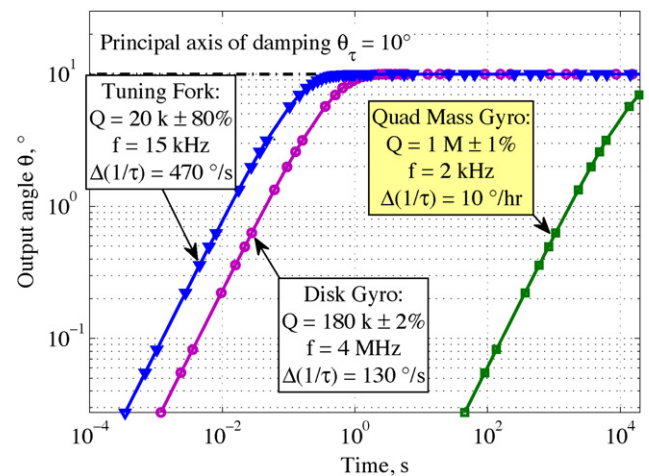


Fig. 10. Drift rates due to the asymmetric damping for tuning fork, disk, and lumped quadruple designs, simulation. For QMG prototype the drift is $1^\circ/\text{h}$, currently limited by fabrication imperfections and packaging.

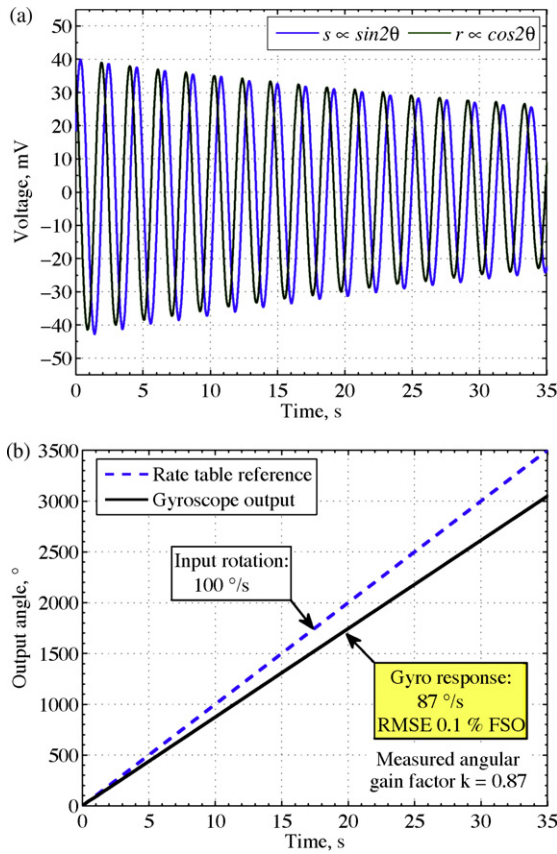


Fig. 11. Experimentally measured angle response of the QMG sensor to a $100^\circ/\text{s}$ rate input using the detection scheme shown in Fig. 6; root mean square (RMS) nonlinearity is below 0.1% of full scale output (FSO). (a) Measured s and r demodulated components of x and y readout signals during an applied $100^\circ/\text{s}$ rotation. (b) Gyro angle output $\theta = \arctan(s/r)/2$ and the rate table reference.

gyroscope response with RMS nonlinearity of below 0.1% full scale output (FSO). The extracted angular gain factor of 0.87 was found to be in excellent agreement with the predicted value of 0.88. For the following experiments we take into account the actual value for $k = 0.87$ when calculating an output angle.

5.2.3. Response to accelerated rotation

The input linear range of the whole-angle mode is fundamentally unlimited due to free, unconstrained precession of the axis of vibration in response to the device rotation. To experimentally confirm linearity, the device was rotated with a constant angular acceleration of $280^\circ/\text{s}^2$, providing input rates of 0 to $450^\circ/\text{s}$ and angular positions of 0 to 350° in 1.4 s, Fig. 12. The amplitude change of X - and Y -modes was recorded in response to this accelerated rotation, Fig. 12(a). Initially, the device was vibrating in X -direction, and after a 90° rotation the proof-mass was oscillating in the Y -direction. The subsequent 90° rotation causes the device to vibrate again in the X -mode. These energy transfers between the X - and Y -modes serve as the basis for the angle detection. The precession angle of the vibration pattern was computed in real time from the amplitudes of X - and Y -modes using the relation $\theta = \arctan(s/r)/(2k)$, Fig. 12(b). The measured angle response confirmed the orientation-independent angular gain, as well as sensor linearity for wide input range of $450^\circ/\text{s}$ with 0.4% RMS error full scale output (limited by the experimental setup), Fig. 12(c).

For applications requiring angular rate information, the numerical differentiation of the measured angle output is possible. The

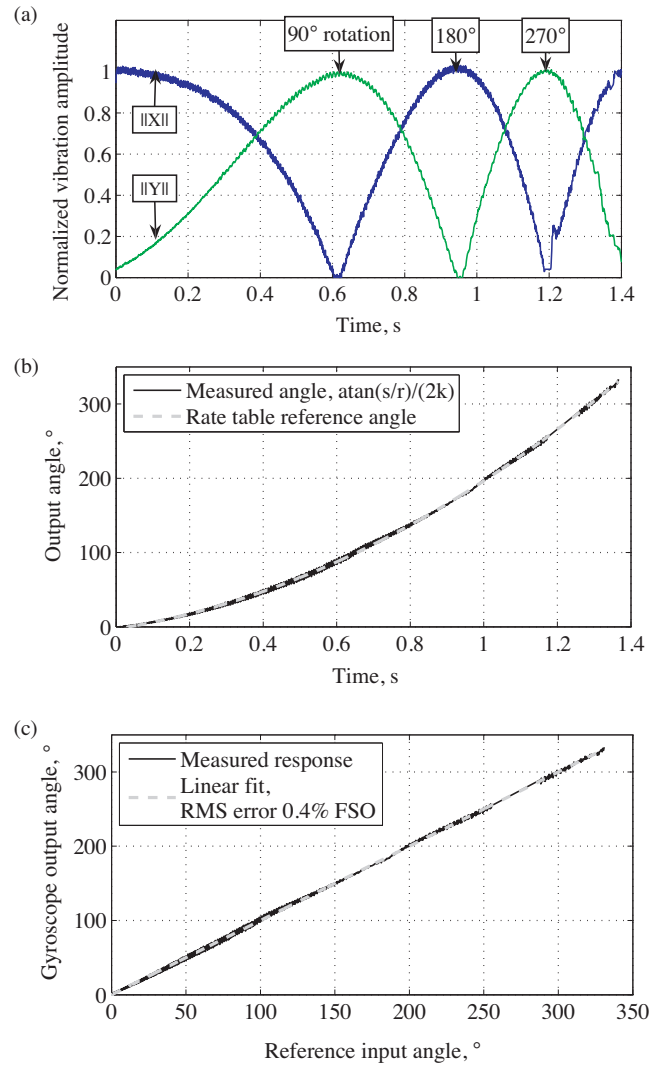


Fig. 12. QMG angle response to a constant angular acceleration of $280^\circ/\text{s}^2$. (a) Measured vibration amplitudes of X - and Y -modes in response to rotation with constant acceleration $280^\circ/\text{s}^2$. (b) Direct angle measurement derived from $\arctan(s/r)/(2k)$. (c) Measured angle response demonstrates sensor linearity.

experimental demonstration is performed by applying a sequence of $\pm 50, \pm 100^\circ/\text{s}$ input rotations to the QMG sensor operated in whole-angle mode, Fig. 13. The measured output angle was computed according to $\theta = \arctan(s/r)/(2k)$, while the angular rate was derived by numerical differentiation of the angle signal. The measured angular rates of $\pm 50, \pm 100^\circ/\text{s}$ (within 0.2% error margin) were found to be in good agreement with the applied input rates.

5.3. Bandwidth analysis

The whole-angle operating mode is also expected to provide unlimited measurement bandwidth. The bandwidth of mode-matched ultra-low dissipation QMG device was characterized for both conventional rate measuring (forced vibrations) and whole-angle modes (free vibrations). Scale factors were measured for periodic rotations with the frequencies up to 100 Hz (limited by the Ideal Aerosmith 1291 BR rate table specifications). Fig. 14 shows the experimentally measured QMG response to a 100 Hz sinusoidal rotation, confirming the robust operation and stable angular gain factor at high rotational frequencies. The output was

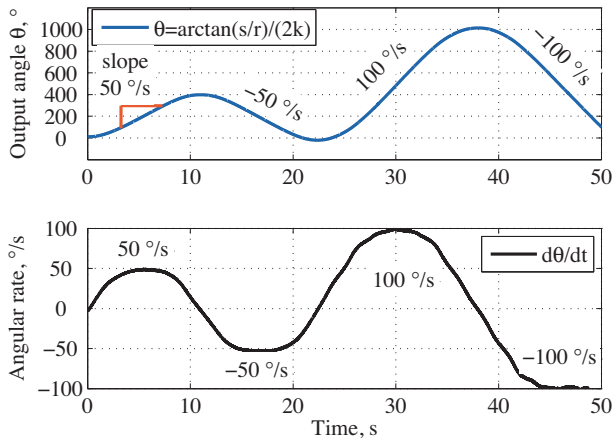


Fig. 13. Measured QMG response to a sequence of ± 50 , $\pm 100^\circ/\text{s}$ input rotations, showing the gyroscope angle output and derived angular rate signal.

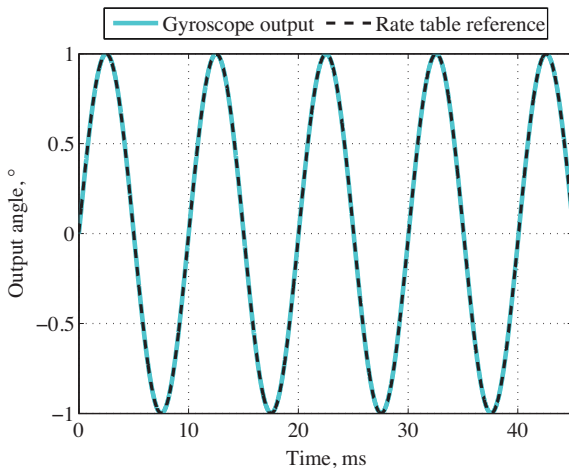


Fig. 14. Measured QMG response to a 100 Hz sinusoidal rotation, confirming the robust operation and stable angular gain factor at high rotational frequencies.

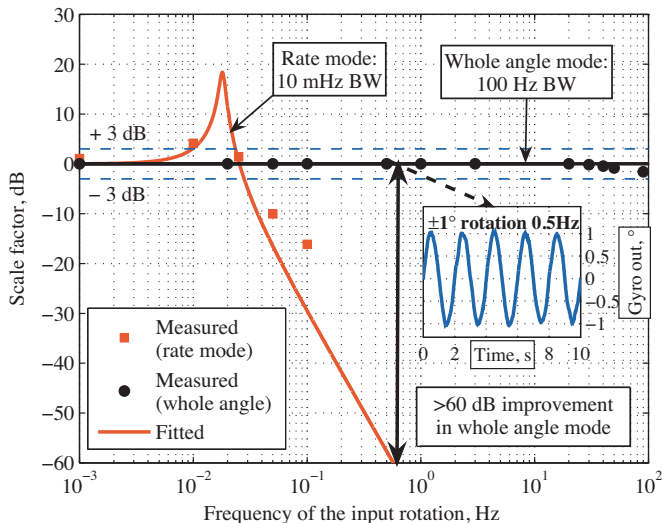


Fig. 15. Experimental comparison of the QMG gyroscope bandwidth, demonstrating 60 dB improvement when operated in the whole-angle mode (over the rate measuring mode).

post-processed using a band-stop (notch) filter with a 60 Hz center frequency to eliminate a.c. power line component. Scale factors of the rate operating mode were normalized to the constant rotation and compared to the angular gain factors of the whole-angle mode, Fig. 15. Characterization of the whole-angle operating mode revealed a bandwidth in excess of 100 Hz, which is a 10,000 improvement over the conventional open-loop rate mode with a 10 mHz bandwidth. The apparent reduction in gain at large input frequencies in Fig. 15 is due to the low-pass filters used in signal processing.

6. Conclusions

We demonstrated the silicon MEMS angle measuring gyroscope enabled by the geometrically symmetric QMG design providing unprecedented ultra-high Q -factors. The vacuum sealed SOI prototype with a 2 kHz operational frequency demonstrated virtually identical X - and Y -mode Q -factors of 1.2 million, approaching the thermoelastic limit of 1.35 million. The temperature characterization revealed isotropic Q -factors above 0.7 million in the range -40°C to $+100^\circ\text{C}$. This allows for a power failure-independent operation with polarization voltages as low as 10 mV dc previously achieved only in HRG for space-flight missions [8]. Due to stiffness and damping symmetry, and ultra-low dissipation, this gyroscope was instrumented for the direct measurements of the angle with fundamentally unlimited input range and bandwidth. Experimental characterization of the mode-matched QMG operating in the whole-angle mode confirmed 0.4% linearity in excess of $\pm 450^\circ/\text{s}$ range and 100 Hz bandwidth, eliminating both bandwidth and range constraints of conventional MEMS vibratory rate gyroscopes. Further experimental characterization of QMG operated in free vibrations confirmed the wide input rate of $\pm 18,000^\circ/\text{s}$ [25]. The measured damping asymmetry $\Delta Q/Q$ of 1% translates to the theoretical angle drift of $1^\circ/\text{h}$ in whole-angle operating mode, making one high- Q mechanical structure suitable for both high precision and wide input range applications. Ongoing improvements in the gyroscopes layout, fabrication, and capacitive pick-off electronic loops are projected to reduce the angle drift to below sub-degree per hour.

Acknowledgment

This work was supported by the Office of Naval Research and Naval Surface Warfare Center Dahlgren Division under Grants N00014-09-1-0424 and N00014-11-1-0483. The authors would like to thank Dr. F. Heer from Zurich Instruments for assistance with interface electronics, B. Simon for aid in finite element modeling, Dr. D. Lynch and Prof. R. M'Closkey for expert suggestions. The gyroscopes were designed, fabricated, and characterized at the MicroSystems Laboratory, University of California, Irvine.

Appendix A. Foucault pendulum dynamics

The classical Foucault pendulum is a large swinging pendulum, which was used by Leon Foucault to demonstrate the Earth's rotation [35]. The pendulum model describes dynamics of both angular rate and angle measuring vibratory gyroscopes. While theory and analysis have been extensively developed in [15,36,6,17,19,23], here we summarize the main results to explain operating principle and to derive gyroscope parameters favorable for direct angle measurements.

A.1. Ideal case

Foucault pendulum can be defined as a 2-D isotropic resonator oscillating with frequency ω . The governing equations of motion in terms of displacements components u and v relative to the non-moving inertial reference frame are:

$$\begin{aligned}\ddot{u} + \omega^2 u &= 0, \\ \ddot{v} + \omega^2 v &= 0.\end{aligned}\quad (\text{A.1})$$

Depending on the initial conditions, Eq. (A.1) describes either a straight line or an elliptical trajectory motion, Fig. 1. When using orbital parameters a , q , θ , ϕ , representing semi-major, semi-minor axes, the precession angle, and the orbital phase, the solution of Eq. (A.1) is:

$$\begin{aligned}u &= a \cos \theta \cos(\omega t + \phi) - q \sin \theta \sin(\omega t + \phi), \\ v &= a \sin \theta \cos(\omega t + \phi) + q \cos \theta \sin(\omega t + \phi).\end{aligned}\quad (\text{A.2})$$

From an instrumentation point of view, a and q are in-phase and in-quadrature components of fast-varying variables u , v relative to the reference phase ϕ . For zero quadrature $q=0$ the gyroscope motion is a straight line in u - v plane; for zero inclination angle $\theta=0$ the line of oscillation is aligned with the u axis:

$$\begin{aligned}u &= a \cos(\omega t + \phi), \\ v &= 0.\end{aligned}\quad (\text{A.3})$$

The coordinate transformation is used to map the solution and equations of motion from the stationary inertial frame to the gyroscope frame of reference, which is rotated by the angle θ (with the angular rate Ω and acceleration $\dot{\Omega}$). The cosine rotation matrix connects the displacement components x , y in the gyroscope frame with the components u , v in the inertial frame:

$$\begin{aligned}u &= x \cos \theta - y \sin \theta, \\ v &= x \sin \theta + y \cos \theta.\end{aligned}\quad (\text{A.4})$$

Substituting Eq. (A.4) to Eq. (A.1), the equations of motion become:

$$\begin{aligned}\ddot{x} + (\omega^2 - \Omega^2)x - 2\Omega\dot{y} - \dot{\Omega}y &= 0, \\ \ddot{y} + (\omega^2 - \Omega^2)y + 2\Omega\dot{x} + \dot{\Omega}x &= 0.\end{aligned}\quad (\text{A.5})$$

Similarly, the general solution of Eq. (A.5) in the rotating gyroscope frame is:

$$\begin{aligned}x &= a \cos \left(\theta_0 - \int_{t_0}^t \Omega(\tau) d\tau \right) \cos(\omega t + \phi) \\ &\quad - q \sin \left(\theta_0 - \int_{t_0}^t \Omega(\tau) d\tau \right) \sin(\omega t + \phi), \\ y &= a \sin \left(\theta_0 - \int_{t_0}^t \Omega(\tau) d\tau \right) \cos(\omega t + \phi) \\ &\quad + q \cos \left(\theta_0 - \int_{t_0}^t \Omega(\tau) d\tau \right) \sin(\omega t + \phi),\end{aligned}\quad (\text{A.6})$$

which represents either a straight line or an orbital trajectory with the initial inclination angle θ_0 relative to x - y plane. Analysis of Eqs. (A.2) and (A.6) shows that the trajectory pattern precesses with the angular rate $-\Omega$ in the gyroscope frame, but remains fixed in the inertial space, thereby providing an inertial reference for orientation angle measurements. In other words, at any time interval $t - t_0$

the variable inclination angle θ of the orbital trajectory is equal to the angle of a gyroscope inertial rotation:

$$\theta = \theta_0 - \int_{t_0}^t \Omega(\tau) d\tau, \quad (\text{A.7})$$

which proves that Foucault pendulum is a rate integrating gyroscope.

For zero quadrature ($q=0$) the solution Eq. (A.6) simplifies to a straight line precession:

$$\begin{aligned}x &= a \cos \left(\theta_0 - \int_{t_0}^t \Omega(\tau) d\tau \right) \cos(\omega t + \phi), \\ y &= a \sin \left(\theta_0 - \int_{t_0}^t \Omega(\tau) d\tau \right) \cos(\omega t + \phi).\end{aligned}\quad (\text{A.8})$$

The angle of an orbital inclination (precession angle) can be directly measured from the x , y displacement components Eq. (A.8) at any time:

$$\arctan \frac{y}{x} = \theta_0 - \int_{t_0}^t \Omega(\tau) d\tau. \quad (\text{A.9})$$

Eq. (A.9) is the governing equation for direct angle measurements of a gyroscope rotation from x , y displacements (as opposed to numerical integration of an angular rate output in conventional gyroscopes). While Eq. (A.7) is true for arbitrary initial conditions, Eq. (A.9) holds as long as the quadrature is minimized to zero, i.e. $q=0$. For non-ideal case the direct angle measurements are also possible; details are discussed in Section 4.

A.2. Non-ideal case

One of the possible physical realizations of Foucault pendulum is a 2-D mass-spring-damper system, which is subject to fabrication imperfections if in MEMS implementation. Considering mismatches between natural frequencies ω_1 , ω_2 :

$$\Delta\omega = \frac{\omega_1^2 - \omega_2^2}{2\omega}, \quad \omega = \frac{\omega_1^2 + \omega_2^2}{2},$$

and mismatches in energy dissipation time constants τ_1 , τ_2 :

$$\Delta \left(\frac{1}{\tau} \right) = \frac{1}{\tau_1} - \frac{1}{\tau_2}, \quad \frac{1}{\tau} = \frac{1/\tau_1 + 1/\tau_2}{2},$$

the realistic model of an angle measuring gyroscope is:

$$\begin{aligned}\ddot{x} + \frac{2}{\tau}\dot{x} + \Delta \left(\frac{1}{\tau} \right) (\dot{x} \cos 2\theta_\tau + \dot{y} \sin 2\theta_\tau) + (\omega^2 - k^2\Omega^2)x \\ - \omega \Delta\omega (x \cos 2\theta_\omega + y \sin 2\theta_\omega) - k(2\Omega\dot{y} + \dot{\Omega}y) &= 0 \\ \ddot{y} + \frac{2}{\tau}\dot{y} - \Delta \left(\frac{1}{\tau} \right) (-\dot{x} \sin 2\theta_\tau + \dot{y} \cos 2\theta_\tau) + (\omega^2 - k^2\Omega^2)y \\ + \omega \Delta\omega (-x \sin 2\theta_\omega + y \cos 2\theta_\omega) + k(2\Omega\dot{x} + \dot{\Omega}x) &= 0,\end{aligned}\quad (\text{A.10})$$

where k is the angular gain factor defined by the geometry of a sensitive element, and θ_τ , θ_ω are the angles of the τ_1 and ω_2 principal axes of damping and elasticity, respectively.

The analysis of non-ideal dynamics is simplified when using slow-varying orbital parameters a , q , θ , ϕ , which are no longer constants but time-varying variables, Fig. 1. Assuming $\omega \gg \Omega$ and using

methods of averaging, Eq. (A.10) becomes [6]:

$$\begin{aligned}\dot{a} &= -\left[\frac{1}{\tau} + \frac{1}{2}\Delta\left(\frac{1}{\tau}\right)\cos 2(\theta - \theta_\tau)\right]a + \frac{1}{2}\Delta\omega\sin 2(\theta - \theta_\omega)q, \\ \dot{q} &= -\left[\frac{1}{\tau} - \frac{1}{2}\Delta\left(\frac{1}{\tau}\right)\cos 2(\theta - \theta_\tau)\right]q - \frac{1}{2}\Delta\omega\sin 2(\theta - \theta_\omega)a, \\ \dot{\theta} &= -k\Omega + \frac{1}{2}\Delta\left(\frac{1}{\tau}\right)\sin 2(\theta - \theta_\tau) + \Delta\omega\cos 2(\theta - \theta_\omega)\frac{aq}{a^2 - q^2}, \\ \dot{\phi} &= -\frac{aq}{a^2 - q^2}\Delta\left(\frac{1}{\tau}\right)\sin 2(\theta - \theta_\tau) - \frac{1}{2}\Delta\omega\cos 2(\theta - \theta_\omega).\end{aligned}\quad (\text{A.11})$$

These equations show that both aniso-damping $\Delta(1/\tau)$ and aniso-elasticity $\Delta\omega$ result in false precession θ of an orbital trajectory with time-varying amplitude a , quadrature q and phase ϕ . Analysis of Eq. (A.11) also reveals that the inclination angle drift $\dot{\theta}$ is periodic, so the precession error is averaged out for fast spinning objects. While aniso-elasticity can be reduced by minimizing the multiplier q , or by electrostatic tuning of $\Delta\omega$, control of aniso-damping is typically challenging. From the other hand, for the isotropic case $\Delta\omega = \Delta(1/\tau) = 0$, the presence of damping τ does not influence the precession:

$$\begin{aligned}\dot{a} &= -\frac{a}{\tau}, \\ \dot{q} &= -\frac{q}{\tau}, \\ \dot{\theta} &= -k\Omega, \\ \dot{\phi} &= 0.\end{aligned}\quad (\text{A.12})$$

Even though both the amplitude and quadrature decay with the rate $\exp(-t/\tau)$, the inclination angle change $\theta - \theta_0$ is proportional at any time interval $t - t_0$ to the inertial rotation angle with the angular gain k :

$$\theta - \theta_0 = -k \int_{t_0}^t \Omega(\tau) d\tau, \quad (\text{A.13})$$

thereby making possible direct angle measurements in free vibrations regime. These considerations support the development of the perfectly symmetrical sensitive element to ensure isotropy in both damping and elasticity, as well as maximization of energy decay time to prolong operation in free decay.

References

- [1] A. Shkel, Type I and type II micromachined vibratory gyroscopes, in: Position, Location, And Navigation Symposium, 2006 ION, 2006, pp. 586–593.
- [2] M. Weinberg, R. Candler, S. Chandorkar, J. Varsanik, T. Kenny, A. Duwel, Energy loss in MEMS resonators and the impact on inertial and RF devices, in: Proc. Solid-State Sensors, Actuators and Microsystems Conference, TRANSDUCERS 2009, International, 2009, pp. 688–695.
- [3] M. Zaman, A. Sharma, Z. Hao, F. Ayazi, A mode-matched silicon-yaw tuning-fork gyroscope with subdegree-per-hour allan deviation bias instability, *Journal of Microelectromechanical Systems* 17 (2008) 1526–1536.
- [4] I. Prikhodko, S. Zotov, A. Trusov, A. Shkel, Sub-degree-per-hour silicon MEMS rate sensor with 1 million Q-factor, in: Proc. 16th International Conference on Solid-State Sensors, Actuators and Microsystems (TRANSDUCERS'11), Beijing, China, 2011, p. 2809–2812.
- [5] I. Prikhodko, A. Trusov, A. Shkel, North-finding with 0.004 radian precision using a silicon MEMS quadruple mass gyroscope with Q-factor of 1 million, in: Proc. IEEE Int. Conf. Micro-Electro-Mechanical Systems 2012, Paris, France, 2012, pp. 164–167.
- [6] D. Lynch, Vibratory gyro analysis by the method of averaging, in: Proc. 2nd St. Petersburg International Conference on Gyroscopic Technology and Navigation, 1995, pp. 26–34.
- [7] A. Shkel, Microtechnology comes of age, in: GPS World, 2011, pp. 43–50.
- [8] D.M. Rozelle, The hemispherical resonator gyro: from wineglass to the planets (AAS 09-176), in: Proc. 19th AAS/AIAA Space Flight Mechanics Meeting, 2009, pp. 1157–1178.
- [9] A.M. Shkel, R.T. Howe, Micro-machined angle measuring gyroscope, U.S. patent 6 481 285 (2002).
- [10] C. Painter, Micromachined Vibratory Gyroscopes with Imperfections, Ph.D. thesis, Univ. of California, Irvine, 2005.
- [11] A. Trusov, I. Prikhodko, S. Zotov, A. Schofield, A. Shkel, Ultra-high Q silicon gyroscopes with interchangeable rate and whole angle modes of operation, in: Proc. Sensors, 2010 IEEE, 2010, pp. 864–867.
- [12] A.A. Trusov, A.R. Schofield, A.M. Shkel, Micromachined tuning fork gyroscopes with ultra-high sensitivity and shock rejection, U.S. patent application 20 100 313 657 (2010b).
- [13] A. Schofield, A. Trusov, A. Shkel, Versatile vacuum packaging for experimental study of resonant MEMS, in: Micro Electro Mechanical Systems (MEMS), IEEE 23rd International Conference, 2010, pp. 516–519.
- [14] I. Prikhodko, S. Zotov, A. Trusov, A. Shkel, Foucault pendulum on a chip: angle measuring silicon MEMS gyroscope, in: Proc. IEEE Int. Conf. Micro-Electro-Mechanical Systems, Cancun, Mexico, 2011, pp. 161–164.
- [15] B. Friedland, M. Hutton, Theory and error analysis of vibrating-member gyroscope, *IEEE Transactions on Automatic Control* 23 (1978) 545–556.
- [16] A. Shkel, R. Horowitz, A. Seshia, S. Park, R. Howe, Dynamics and control of micro-machined gyroscopes, in: American Control Conference, 1999, Proceedings of the 1999, vol. 3, 1999, pp. 2119–2124.
- [17] C. Painter, A. Shkel, Active structural error suppression in MEMS vibratory rate integrating gyroscopes, *Sensors Journal* IEEE 3 (2003) 595–606.
- [18] D. Piyabongkarn, R. Rajamani, M. Greminger, The development of a MEMS gyroscope for absolute angle measurement, *IEEE Transactions on Control Systems Technology* 13 (2005) 185–195.
- [19] S. Park, R. Horowitz, C.-W. Tan, Dynamics and control of a MEMS angle measuring gyroscope, *Sensors and Actuators A: Physical* 144 (2008) 56–63.
- [20] B.J. Gallacher, Principles of a Micro-Rate Integrating Ring Gyroscope, *IEEE Transactions on Aerospace and Electronic Systems* 48 (1) (2012) 658–672.
- [21] J. Gregory, J. Cho, K. Najafi, MEMS rate and rate-integrating gyroscope control with commercial software defined radio hardware, in: 16th International Solid-State Sensors, Actuators and Microsystems Conference (TRANSDUCERS'11), 2011, pp. 2394–2397.
- [22] G. Bryan, On the beats in the vibrations of a revolving cylinder or bell, in: Proc. of Cambridge Phil. Soc., vol. VII, pp. 101–111.
- [23] D. Lynch, Coriolis vibratory gyros, in: Symposium Gyro Technology 1998, pp. 1.0–1.14. (Reproduced as Annex B, Coriolis Vibratory Gyros, pp. 56–66 of IEEE Std. 1431-2004, IEEE Standard Specification Format Guide and Test Procedure of Coriolis Vibratory Gyros, IEEE Aerospace and Electronic Systems Society, 20 December, 2004).
- [24] A. Sharma, M. Zaman, F. Ayazi, A sub-0.2 deg/h bias drift micromechanical silicon gyroscope with automatic CMOS mode-matching, *IEEE Journal of Solid-State Circuits* 44 (2009) 1593–1608.
- [25] S.A. Zotov, A.A. Trusov, A.M. Shkel, Demonstration of a wide dynamic range angular rate sensor based on frequency modulation, in: Proc. IEEE Sensors 2011, Limerick, Ireland, Oct. 28–31, 2011, pp. 149–152.
- [26] M. Kranz, G. Fedder, Micromechanical vibratory rate gyroscopes fabricated in conventional CMOS, in: Proc. Symposium Gyro Technology, Stuttgart, Germany, 1997, pp. 3.0–3.8.
- [27] J. Bernstein, S. Cho, A. King, A. Kourepenis, P. Maciel, M. Weinberg, A micromachined comb-drive tuning fork rate gyroscope, in: Proc. IEEE Micro Electro Mechanical Systems Conference (MEMS '93), 1993, pp. 143–148.
- [28] M. Weinberg, J. Connelly, A. Kourepenis, D. Sargent, Microelectromechanical instrument and systems development at the Charles Stark Draper Laboratory, inc, in: Digital Avionics Systems Conference, 16th DASC., AIAA/IEEE, vol. 2, 1997, pp. 8.5-33–8.5-40.
- [29] A. Kourepenis, J. Borenstein, J. Connelly, R. Elliott, P. Ward, M. Weinberg, Performance of MEMS inertial sensors, in: Position Location and Navigation Symposium, IEEE, 1998, pp. 1–8.
- [30] R. Candler, H. Li, M. Lutz, W.-T. Park, A. Partridge, G. Yama, T. Kenny, Investigation of energy loss mechanisms in micromechanical resonators, in: TRANSDUCERS, 12th International Conference on Solid-State Sensors, Actuators and Microsystems, 2003, vol. 1, 2003, pp. 332–335.
- [31] B. Kim, M. Hopcroft, R. Candler, C. Jha, M. Agarwal, R. Melamud, S. Chandorkar, G. Yama, T. Kenny, Temperature dependence of quality factor in MEMS resonators, *Journal of Microelectromechanical Systems* 17 (2008) 755–766.
- [32] C.-C. Nguyen, Micromechanical Signal Processors, Ph.D. thesis, Univ. of California, Berkeley, 1994.
- [33] S. Zotov, I. Prikhodko, A. Trusov, A. Shkel, Frequency modulation based angular rate sensor, in: Proc. IEEE Int. Conf. Micro-Electro-Mechanical Systems 2011, Cancun, Mexico, 2011, pp. 577–580.
- [34] Z. Hu, B. Gallacher, J. Burdett, C. Fell, K. Townsend, Precision mode matching of MEMS gyroscope by feedback control, in: Sensors, 2011 IEEE, 2011, pp. 16–19.
- [35] L. Foucault, Sur un nouvelle demonstration experimentale du mouvement de la terre fondee sur la fixite du plan de rotation, *Comptes Rendus De L. Academie Des Sciences* 35 (1852) 421.
- [36] M.W. Putty, A Micromachined Vibrating Ring Gyroscope, Ph.D. thesis, Univ. of Michigan, Ann Arbor, 1995.
- [37] A.A. Trusov, I.P. Prikhodko, S.A. Zotov, A.M. Shkel, Low-Dissipation Silicon Tuning Fork Gyroscopes for Rate and Whole Angle Measurements, *IEEE Sensors Journal* 11 (11) (2011) 2763–2770.
- [38] S. Sonmezoglu, S.E. Alper, T. Akin, in: Proc. IEEE Int. Conf. Micro-Electro-Mechanical Systems 2012, Paris, France, An automatically mode-matched MEMS gyroscope With 50 Hz bandwidth (2012) 523–526.

Biographies

Igor P. Prikhodko received the B.S. and M.S. degrees (cum laude) in applied mathematics and mechanics from the Moscow State University, Moscow, Russia, in 2007, and the M.S. degree in mechanical and aerospace engineering from the University of California, Irvine, in 2008. Currently, he is working towards the Ph.D. degree at the MicroSystems Laboratory, University of California, Irvine. His primary research focus is full-cycle research and development of inertial micromachined sensors, reflected in 4 journal and 15 international conference papers. He is a recipient of the 2008 Holmes Fellowship Award and the 2011 Outstanding Paper Award at the Transducers conference. He is a member of the Institute of Electrical and Electronics Engineers (IEEE), the American Society of Mechanical Engineers (ASME), and serves as a reviewer for major MEMS journals.

Sergei A. Zotov received the M.S. and Ph.D. degrees in mechanical engineering and control systems from the Tula State University, Tula, Russia, in 1999 and 2002, respectively. He is currently a Postdoctoral Scientist at the MicroSystems Laboratory, University of California, Irvine, where he is responsible for the design, fabrication, and testing of micromachined devices and systems for inertial navigation. He holds eight Russian patents and three U.S. patents pending. Over the last ten years his focus has been on MEMS accelerometers and gyroscopes. He is a member of the Institute of Electrical and Electronics Engineers (IEEE).

Alexander A. Trusov received the B.S. and M.S. degrees in applied mathematics and mechanics from the Moscow State University, Moscow, Russia, in 2004, and the M.S. and Ph.D. degrees in mechanical and aerospace engineering from the University of

California, Irvine, in 2006 and 2009, respectively. He is currently a Project Scientist at the UC Irvine MicroSystems Laboratory, where he serves as a PI and Co-PI on a variety of federally sponsored programs pursuing high-performance inertial microsystems. He has published over 40 journal and conference papers on MEMS and inertial sensors, has seven pending U.S. patents, and serves as a reviewer for major journals in the fields of MEMS and sensors. His research interests include design, modeling, fabrication, and vacuum packaging of micromachined inertial systems, design of characterization experiments, and statistical data processing and analysis. He is a member of the Institute of Electrical and Electronics Engineers (IEEE) and the American Society of Mechanical Engineers (ASME). He is a recipient of an Outstanding Paper Award on low-dissipation silicon MEMS gyroscopes at the Transducers 2011 Conference.

Andrei M. Shkel received the diploma degree (With Excellence) in mechanics and mathematics from the Moscow State University, Moscow, Russia, in 1991, and the Ph.D. degree in mechanical engineering from the University of Wisconsin, Madison, in 1997. He is a program manager in the Microsystems Technology Office of the Defense Advanced Research Projects Agency (DARPA), Arlington, VA. He is serving in this capacity while on leave from his faculty position as a professor in the Department of Mechanical and Aerospace Engineering at the University of California, Irvine, where he is also the Director of the UCI Microsystems Laboratory. He is the holder of 15 U.S. and international patents. His professional interests are reflected in more than 120 publications. He is a recipient of the 2009 Research Award from the IEEE Sensors Council, the 2006 UCI Research Award, the 2005 NSF CAREER Award, and the 2002 George E. Brown, Jr., Award. He is an editor of the *Journal of Microelectromechanical Systems* (JMEMS).